ACS APPLIED MATERIALS & INTERFACES

RESEARCH ARTICLE

www.acsami.org

Self-Templating Synthesis of SnO_2—Carbon Hybrid Hollow Spheres for Superior Reversible Lithium Ion Storage

Ping Wu, Ning Du,* Hui Zhang, Chuanxin Zhai, and Deren Yang

State Key Lab of Silicon Materials and Department of Materials Science and Engineering, Zhejiang University, Hangzhou 310027, People's Republic of China

ABSTRACT: This paper reports a novel self-templating methodology for the formation of SnO_2-carbon hybrid hollow spheres by using Sn spheres as sacrificing templates. The time-sequenced structural evolution of the templates indicates that the nanoscale Kirkendall effect plays a critical role in the transformation from Sn spheres to the hybrid hollow spheres. Moreover, the as-synthesized SnO_2—carbon hybrid hollow spheres have been applied as anode materials for lithium-ion batteries, which exhibit a much higher initial Coulombic efficiency and better cycling performance than pure SnO_2 hollow spheres.

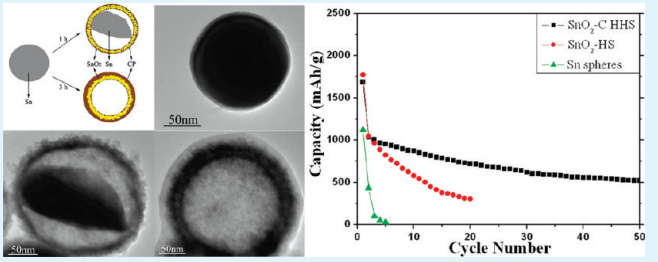

KEYWORDS: self-templating synthesis, nanoscale Kirkendall effect, SnO_2, carbon, hybrid hollow spheres, lithium ion batteries

1. INTRODUCTION

Hollow micro/nanospheres have attracted significant attention because of their unique chemical, optical, electrical, and magnetic properties that are distinctively different from their bulk counterparts.[1−6] Owing to their low density, high surface area, and porous structures, various types of hollow spheres including carbon,[2] Au,[3] MnO_2,[4] CdS,[5] and ZnV_2O_4[6] are found to show high performance in bilirubin adsorbents, water treatment, sensors, lithium-ion batteries, and so forth. Furthermore, hybrid hollow spheres, which contain multiple functional components, are expected to show novel properties or improved performance in a variety of applications compared to single-component hollow spheres.[7−11] For example, Yu et al. obtained novel optical properties from ZnO—dye hollow spheres.[8] Teng et al. synthesized Mn_3O_4—Co_3O_4 hollow spheres with a stronger chemiluminescence intensity and a higher catalytic activity for CO oxidation than single Co_3O_4 ones.[10]

As an important n-type wide bandgap semiconductor, tin dioxide (SnO_2) has received considerable attention over the past few decades because of its unique physicochemical properties and potential applications in gas sensors,[12] transparent electrodes,[13] photocatalysts,[14] and lithium-ion batteries.[15] Among various micro/nanostructures, SnO_2 hollow spheres are of particular interest for reversible lithium ion storage because of their large surface area, short solid-state diffusion length, and excellent toleration for large volume change during cycling.[16−18] Moreover, hybrid SnO_2 hollow spheres, such as SnO_2-α-Fe_2O_3,[19] SnO_2—V_2O_5,[20] and so forth,[21−24] have been demonstrated to exhibit a higher initial Coulombic efficiency and better cycling performance than pure SnO_2 hollow spheres. Among them, SnO_2-carbon hybrid hollow spheres are the most intensively studied ones due to the introduction of carbon component with high electronic conductivity and excellent buffering effect.[21−24] However, the synthetic routes for these hybrid hollow spheres often involve the formation of silica[21,23] or carbon[24] spheres as hard templates, which induces additional template-removing process and production cost of the templates. Therefore, these hard-templating routes seem to be not suitable for the mass production and practical application of the hybrid hollow spheres. It is desirable to obtain the products through more facile and economic procedures.

Herein, we develop a novel self-templating methodology for the formation of SnO_2-carbon hybrid hollow spheres (SnO_2—C HHS) by using Sn spheres as sacrificing templates. The time-sequenced structural evolution of the templates has also been investigated. It is indicated that the nanoscale Kirkendall effect plays a critical role in the transformation from Sn spheres to the hybrid hollow spheres. Moreover, the as-synthesized SnO_2—C HHS have been applied as anode materials for lithium-ion batteries, which show improved lithium-storage performance than pure SnO_2 hollow spheres and pristine Sn spheres.

2. EXPERIMENTAL SECTION

Synthesis of SnO_2—C HHS. The precursor Sn spheres used as sacrificing templates were prepared through a simple polyol method. In a typical synthesis, 0.7 g of PVP was dissolved in 45 mL of DEG at room temperature. The solution was heated up to 170 °C, after which 5 mmol of $SnCl_2$ was added. A freshly prepared solution of $NaBH_4$ (0.872 g in 8 mL of DEG) was then added dropwise with stirring. After 12−15 min at 170 °C, the spheres were centrifuged, washed with ethanol, and finally dried at 80 °C under a vacuum.

SnO_2—C HHS were prepared by a simple hydrothermal carbonization approach.[25,26] Briefly, 0.2 g Sn spheres were dispersed in 40 mL 0.25 M aqueous glucose solution under mild sonication. Then, the solution

Received: February 8, 2011
Accepted: May 3, 2011
Published: May 03, 2011

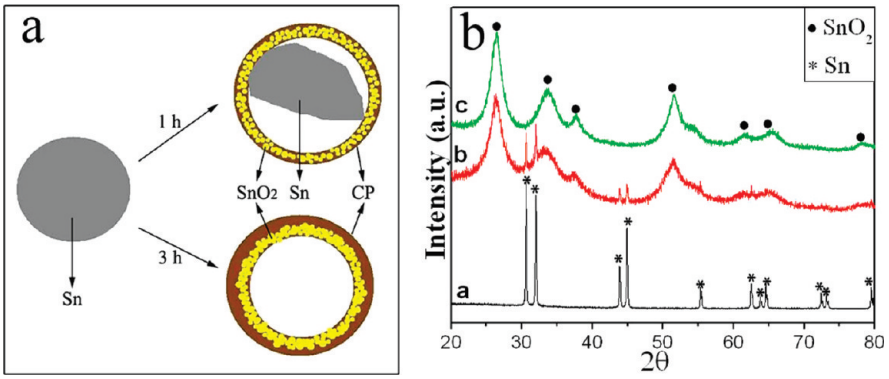

Figure 1. (a) Schematic diagram for the growth process of SnO_2−CP HHS during a hydrothermal treatment; (b) XRD patterns of Sn spheres (curve a), Sn-SnO_2−CP HHS (curve b), and SnO_2−CP HHS (curve c).

was transferred into a 50 mL Teflon-lined stainless steel autoclave, sealed, and maintained at 180 °C for 1 and 3 h, respectively. After the reaction was finished, the resulting brown solid products were centrifuged, washed with distilled water and ethanol, and then dried at 80 °C under vacuum. Finally, the brown products were kept in a tube furnace at 500 °C for 3 h, under nitrogen and in air, respectively, at a ramping rate of 5 °C min^{-1}.

Characterization. The obtained samples were characterized by X-ray powder diffraction (XRD) using a Rigaku D/max-ga X-ray diffractometer with graphite monochromatized Cu Kα radiation (γ = 1.54178 Å). The morphology and structure of the samples were examined by field emission scanning electron microscopy (FESEM, Hitachi S-4800) with energy-dispersive X-ray spectrometer (EDX, Horiba, 7593-H) and transmission electron microscopy (TEM, PHILIPS CM200UT). The FESEM samples were obtained by placing a drop of a suspension of the powders in ethanol on a copper-foil tape. After the evaporation of ethanol, the copper tape was attached to a FESEM aluminum stub. Samples for TEM were prepared by placing a droplet of the suspension onto a Cu-grid with holey carbon film. The Fourier transform infrared (FT-IR) spectra were carried out on an Avatar 360 FT-IR spectrometer. Thermogravimetric analysis (TGA) was tested on an SDT Q600 V8.2 Bulid 100.

Electrochemical Measurements. Electrochemical measurements were carried out using two-electrode 2025 type coin cells with lithium metal as the counter electrodes. The working electrodes were composed of active material (e.g., SnO_2−C HHS), conductive materials (acetylene black, AB), and binder (polyvinyldifluoride, PVDF) in a weight ratio of SnO_2−C HHS/AB/PVDF = 80:10:10, and pasted on a copper foil. Carbon layer in SnO_2−C HHS was considered as active material. The amount of active material loading on each copper foil (about 13 mm in diameter) was around 2 mg. The electrolyte solution was 1 M $LiPF_6$ dissolved in a mixture of ethylene carbonate (EC), propylene carbonate (PC), and diethyl carbonate (DEC) with the volume ratio of EC/PC/DEC = 3:1:1. The cell assembly was performed in a glovebox filled with pure argon (99.999%) in the presence of an oxygen scavenger and a sodium-drying agent. The electrode capacity was measured by a galvanostatic discharge−charge method at a current density of 100 mA g^{-1} in the potential range of 0.01−2 V at 20 °C. Cyclic voltammetry (CV) were recorded on a MSTAT4 (Arbin Instruments) system in the potential range of 0.0−2.0 V at a scan rate of 0.1 mV s^{-1}.

3. RESULTS AND DISCUSSION

SnO_2−C HHS have been prepared through a facile self-templating hydrothermal carbonization methodology by using Sn spheres as sacrificing templates. The self-templating methodology presented here has several advantages compared to the previous reported hard-templating methods.[21−24] First, the preparation of Sn spheres is facile and scalable. Second, the using of Sn spheres as sacrificing templates can avoid the difficulty of removing templates such as silica,[21,23] carbon spheres,[24] and so forth. Third, SnO_2 and carbon precursor (CP) components are introduced into the products through a one-pot hydrothermal process, which further simplify the formation process. Therefore, the self-templating methodology demonstrated here facilitates the mass production and practical application of SnO_2−C HHS.

The effect of hydrothermal time on the phase and morphology changes of the products has been investigated. As schematically illustrated in Figure 1a, Sn spheres have been first converted to Sn-SnO_2 hollow spheres within 1 h of the hydrothermal treatment. In addition, this evolution is accompanied by deposition of a CP layer which is derived from glucose, resulting in Sn-SnO_2−CP hybrid hollow spheres (Sn−SnO_2−CP HHS). When the hydrothermal time increases to 3 h, the precursors have been fully converted to SnO_2−CP HHS with a thicker CP layer. Figure 1b shows the XRD patterns of the products along with the reaction time. As observed, the phase of the products has transformed from tetragonal Sn (curve a) to mixture of Sn and SnO_2 (curve b), and finally to pure tetragonal SnO_2 (curve c), while the CP layer is not well-crystallized.

Figure 2 shows the TEM images of the Sn spheres, Sn−SnO_2−CP HHS, and SnO_2−CP HHS. As observed from Figure 2a,b, the sacrificing precursor has a sphere-like morphology with a diameter of about 100 nm. After a glucose-assisted hydrothermal process, the Sn sphere has been partially oxidized to Sn-SnO_2−CP HHS (Figure 2c,d), then fully oxidized to SnO_2−CP HHS (Figure 2e,f) because of the existence of oxygen dissolved in water. Since the first report by Alivisatos et al,[27] the nanoscale Kirkendall effect has been widely employed for the formation of hollow nanoparticles and nanotubes,[28−30] because the mutual diffusion rates of two components in a diffusion couple differ by a considerable amount.[31] Similar to the previous reports,[27−30] the time-sequenced structural evolution of the products also gives strong evidence of the critical role of nanoscale Kirkendall effect in the transformation from Sn spheres to SnO_2−CP HHS. The formation mechanism of the hollow spheres can be descried as follows. Metallic Sn diffuses outward faster than oxygen inward,[30] leading to the generation of voids between the Sn core and SnO_2 shell. The TEM images of the partially hollow Sn−SnO_2−CP HHS (Figure 2c,d) clearly reveal the voids between the core and shell, which have also been observed in intermediate stages for the formation of hollow

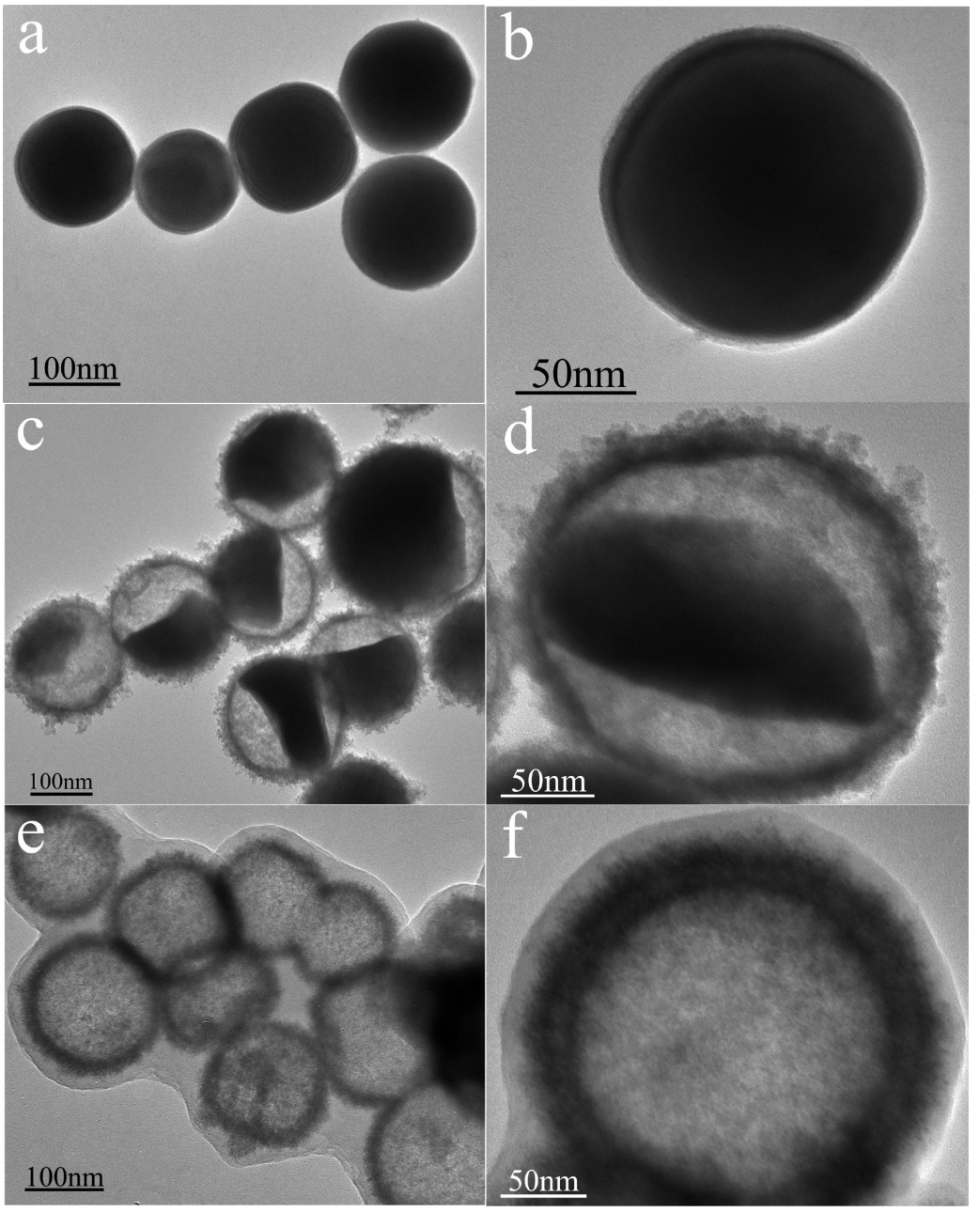

Figure 2. TEM images of (a, b) Sn spheres, (c, d) Sn-SnO_2−CP HHS, and (e, f) SnO_2−CP HHS.

nanostructures in previous reports.[27−30] With prolonged reaction times, all of the remaining Sn core can diffuse into the SnO_2 shell and be oxidized into SnO_2 by oxygen, resulting in SnO_2−CP HHS (Figure 2e,f). In addition, the SnO_2 component in SnO_2−CP HHS exists in the form of accumulation of nanocrystallites with small diameters (∼5 nm), which is consistent with the average crystallite size calculated from the XRD pattern (Figure 1b, curve *c*).

The CP layer, which is derived from glucose under the hydrothermal treatment, can be fully carbonized into carbon layer under inert atmosphere when the annealing temperature is higher than 400 °C.[32] Herein, SnO_2−C HHS were obtained when SnO_2−CP HHS were calcinated under nitrogen at 500 °C. IR spectroscopy was employed to confirm the transition. It can be seen from Figure 3 (curve *a*) that the peak at 1700 cm^{-1} can be attributed to C═O vibration, which comes from polysaccharide in CP layer, suggesting the aromatization of glucose during hydrothermal treatment.[26,33] The peak disappears after carbonization (curve *b*), indicating the full transformation from CP to carbon. In addition, the peaks at about 600 cm^{-1} can be attributed to Sn−O−Sn vibrations, which originate from SnO_2 in the products.[34]

Figure 4 displays the morphological, structural and compositional characterizations of SnO_2−C HHS. As observed from Figure 4a, the SnO_2−C HHS show the sphere-like morphology with hollow structure and continuous carbon layer. The magnified TEM image (Figure 4b) indicates the uniform distribution of SnO_2 nanocrystallites on the interior surface of a hollow carbon sphere. Figure 4c shows the EDX spectrum of the products. As observed, the strong peaks for C, Sn, and O elements are

detected which are expected from carbon and SnO_2 layer, respectively, whereas the peaks for Cu come from the copper tape used in FESEM measurements. HRTEM was also employed to further characterize the products. The HRTEM image (Figure 4d) shows that there are two kinds of lattice fringes with the lattice spacings of about 0.335 and 0.264 nm, corresponding to the (110) and (101) planes of SnO_2 nanocrystallites, respectively.

Pure SnO_2 hollow spheres (SnO_2 HS) were obtained when SnO_2−CP HHS were calcinated in air instead of under nitrogen at 500 °C. Figure 5 shows the morphological, structural and compositional characterizations of pure SnO_2 HS. As can be seen from Figure 5a,b, the carbon layer disappears during the thermal treatment, leaving the bare SnO_2 HS. The average crystallite size in pure SnO_2 HS calculated from the XRD pattern (Figure 5d) increases to about 14 nm, because of the removal of the protecting carbon layer. In addition, there are some broken spheres shown in Figure 5b, further confirming the hollow structure of the products. Figure 5c shows the EDX spectrum of pure SnO_2 HS. As observed, the strong peak for C element disappears in pure SnO_2 HS compared to SnO_2−C HHS (Figure 4c). TGA was performed to determine the amount of carbon presented in SnO_2−C HHS. As can be seen from Figure 6, the weight loss between 200 and 600 °C could be attributed mainly to the removal of carbon layer. Thus, the amount of carbon presented in SnO_2−C HHS is determined to be about 26.4% by weight.

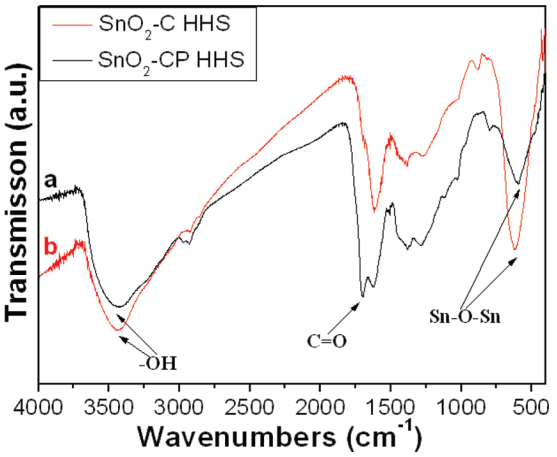

Figure 3. Infrared spectra of SnO_2−CP HHS (curve a) and SnO_2−C HHS (curve b).

The lithium storage property of SnO_2−C HHS as anode materials was investigated at a current density of 100 mA g^{-1} in the potential range of 0.01−2 V (versus Li/Li^+). For comparison, the pristine Sn spheres and pure SnO_2 HS were also investigated under the same conditions. Figure 7 displays the first, second, 10th, 20th, and 50th discharge curves and the first three cyclic voltammogram (CV) curves of the SnO_2−C HHS anode. As observed, the profiles of these discharge and CV curves are characteristics of SnO_2-based anodes.[22,35] It is generally accepted that the electrochemical reaction mechanism of SnO_2-based anodes can be described as irreversible and reversible processes: $SnO_2 + 4Li^+ + 4e^- \rightarrow Sn + 2Li_2O$ (1); $Sn + xLi^+ + xe^- \leftrightarrow Li_xSn$ ($0 \le x \le 4.4$) (2). Thus, the theoretical capacity of SnO_2 anode determined by the reversible process is 781 mA h g^{-1} (4.4 Li). Herein, the discharge capacity of SnO_2−C HHS anode in the second cycle is 1034 mA h g^{-1}, which is much higher than the theoretical capacity of SnO_2 anode. The reason may be as follows. The reduction of SnO_2 to Sn is partially reversible in the SnO_2−C HHS anode, which can explain the extra reversible capacities in SnO_2 anodes. Similar phenomena have been observed in nanostructured SnO_2-based anodes by different groups.[32,35,36] The CV curves of the SnO_2−C HHS anode (Figure 7b) further confirm the partial reversibility of

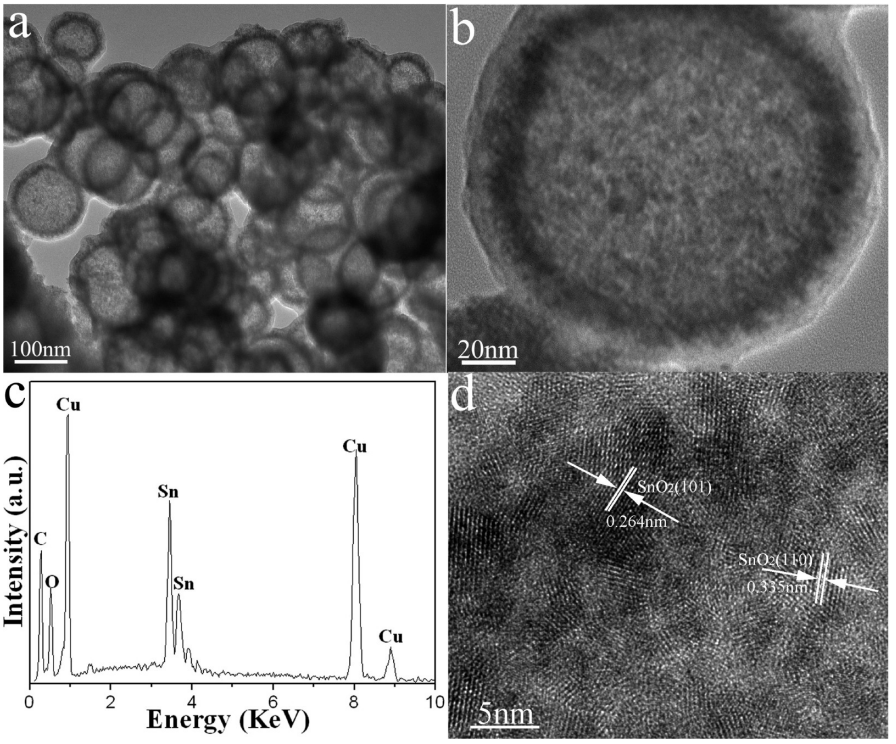

Figure 4. Morphological, structural and compositional characterizations of SnO_2−C HHS: (a,b) TEM images; (c) EDX spectrum; (d) HRTEM image.

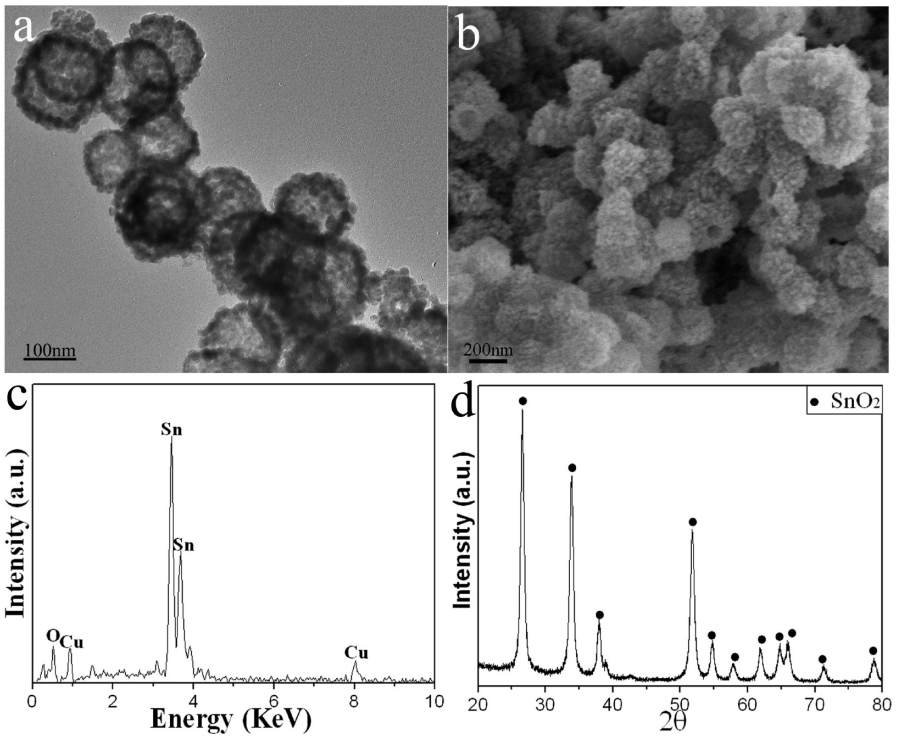

Figure 5. Morphological, structural, and compositional characterizations of pure SnO_2 HS: (a) TEM image; (b) SEM image; (c) EDX spectrum; (d) XRD pattern.

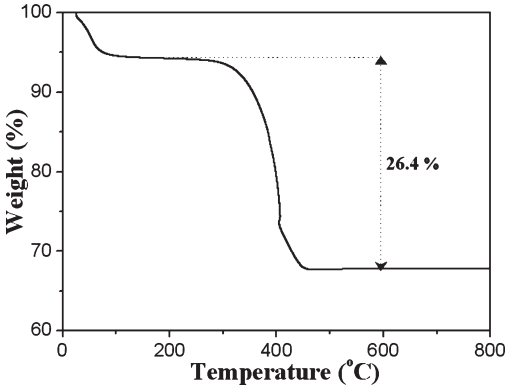

Figure 6. TGA analysis of SnO_2−C HHS.

the reduction process. As observed, the characteristic pair (cathodic, anodic) of current peaks at the potential of (0.8, 1.3 V), which corresponds to the reduction and oxidation processes respectively, still appears in the second and third cycles, suggesting partial reversibility of the reduction of SnO_2 to Sn. Figure 8a shows the discharge and charge capacities as well as Coulombic efficiency as a function of cycle number for the SnO_2−C HHS anode. The initial charge capacity (1002.5 mA h g^{-1}) is much lower than the initial discharge capacity (1685.7 mA h g^{-1}) due to the formation of solid electrolyte interface (SEI) layer and partially reversible reduction of SnO_2 to Sn. Despite this, the initial Coulombic efficiency (59.5%) of SnO_2−C HHS is higher than those of pure SnO_2 HS (47.4%) and previously reported SnO_2-α-Fe_2O_3 hollow spheres (56%).[19] Moreover, the SnO_2−C HHS anode is able to exhibit a high reversible capacity of 521.9 mA h g^{-1} after 50 cycles, which is much higher than the theoretical capacity of graphite (372 mA h g^{-1}) and that of the previously reported SnO_2-carbon hollow spheres (473 mA h g^{-1}).[22] The superior performance of SnO_2−C HHS anode facilitates its application in high-power lithium ion batteries.

Figure 8b compares the cycling performances of SnO_2−C HHS, pure SnO_2 HS, and pristine Sn spheres as anode materials for lithium-ion batteries. As observed, the SnO_2−C HHS anode exhibits markedly improved cycling performance than SnO_2 HS anode. It is widely accepted that the structural stability of micro/nanoanode materials during cycling plays a critical role in their electrochemical performances, especially the cycling performances. The aggregation and pulverization of tin-based particles in SnO_2 HS during cycling, which leads to the breakdown of the electrode structure, can be responsible for the poorer cycling performance. In sharp contrast, the pulverization of the electrode material in SnO_2−C HHS anode is suppressed by the hollow carbon shell. The initial capacity fading (up to 30 cycles) of SnO_2−C HHS anode can be partly ascribed to the little pulverization of the tin-based particles within single hollow sphere.[37] However, the pulverization of the inner tin-based particles can not destroy the structure of SnO_2−C HHS anode because there is enough void space to buffer the huge volume expansion, which can be further confirmed by the morphology of electrode materials after cycling. Figure 9 shows the morphological and structural characterizations of the SnO_2−C HHS anode in a fully delithiated (charge) state after 5 discharge/charge cycles. As observed from Figure 9a, the carbon-coated hollow morphology can be retained, indicating excellent buffering effect of the hollow structure and carbon matrix. In addition, the carbon matrix in SnO_2−C HHS after carbonization has a quite high electronic conductivity, which also facilitates its application in reversible lithium ion storage.[38] Moreover, the crystallographic structure of SnO_2−C HHS in a fully delithiated state was also investigated by XRD measurement (Figure 9b). As observed, the

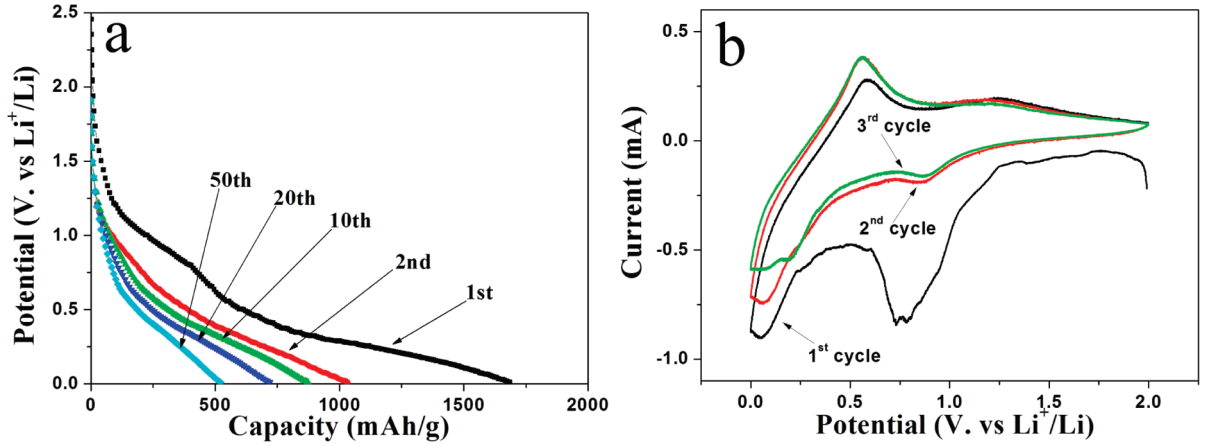

Figure 7. (a) first, second, 10th, 20th, and 50th discharge curves of SnO_2−C HHS anode; (b) first three CV curves of SnO_2−C HHS anode in the potential range of 0.0−2.0 V at a scan rate of 0.1 mV s^{-1}.

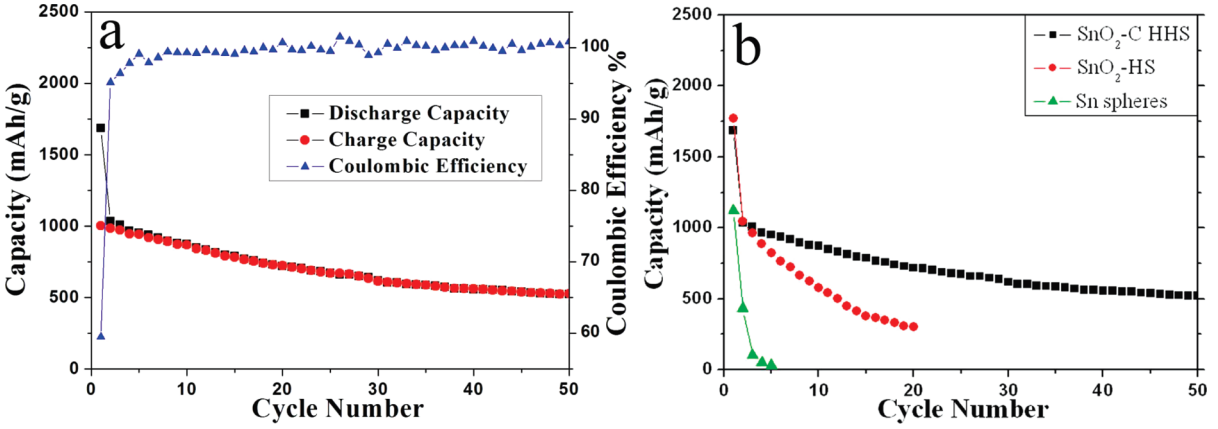

Figure 8. (a) Discharge and charge capacities as well as Coulombic efficiency as a function of cycle number for the SnO_2−C HHS anode at a current density of 100 mA g^{-1} in the potential range of 0.01−2 V at 20 °C; (b) cycling performances of SnO_2−C HHS, pure SnO_2 HS, and pristine Sn spheres as anode materials for lithium-ion batteries.

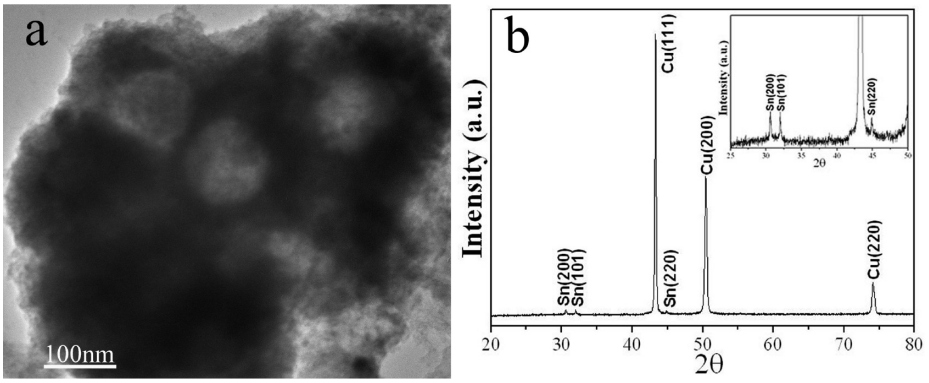

Figure 9. Morphological and structural characterizations of the SnO_2−C HHS anode in a fully delithiated state after 5 discharge/charge cycles: (a) TEM image; (b) XRD pattern with an enlarged inset.

three strong peaks which can be indexed to metallic Cu come from the Cu foil used in battery test, while the other three small peaks (Figure 9b, inset) can be indexed to metallic Sn. The existence of Sn in electrode materials after cycling further confirms the reduction of SnO_2 to Sn during cycling (the first discharge process), which is widely accepted for SnO_2-based anodes.[21−24] Therefore, the novel structure of SnO_2−C HHS anode, which has a higher electronic conductivity and enhanced stability during cycling, may be responsible for the higher initial Coulombic efficiency and better cycling performance than pure SnO_2 HS anode.

Recently, Sn-based anode materials are also believed to be suitable candidates for application in lithium ion batteries since they suffer lower irreversible capacity loss in the first cycle than SnO_2 does.[37,39,40] However, pure Sn materials exhibit very poor cycling performance. As observed from Figure 6, the cycling performance of pristine Sn spheres is even much worse than that of pure SnO_2 HS which has Li_2O as buffering matrix during cycling. So, specific protecting layer, such as silica or carbon, may be needed to solve this problem. Herein, the transformation from Sn spheres to SnO_2−C HHS is also of scientific interest and technological importance for application in lithium ion batteries.

4. CONCLUSIONS

In summary, we have synthesized SnO_2−C HHS through a facile self-templating hydrothermal carbonization approach, in which Sn spheres are used as sacrificing templates. The time-sequenced structural evolution of the templates indicates that nanoscale Kirkendall effect plays the key role in the transformation from Sn spheres to SnO_2−C HHS. Moreover, the as-synthesized SnO_2−C HHS have been applied as anode materials for lithium-ion batteries, which exhibit a much higher initial Coulombic efficiency (59.5%) and improved cycling performance compared to pure SnO_2 HS anode. The SnO_2−C HHS anode is able to exhibit a high reversible capacity of 521.9 mA h g^{-1} at a current density of 100 mA g^{-1} after 50 cycles.

AUTHOR INFORMATION

Corresponding Author
*E-mail: dna1122@zju.edu.cn.

ACKNOWLEDGMENT

The authors appreciate the financial support from 973 Project (2007CB613403), 863 Project (2007AA02Z476), NSFC (No. 50802086), China Postdoctoral Science Foundation funded project (20090461350).

REFERENCES

(1) Lou, X. W.; Archer, L. A.; Yang, Z. *Adv. Mater.* **2008**, *20*, 3987.
(2) Guo, L.; Zhang, L.; Zhang, J.; Zhou, J.; He, Q.; Zeng, S.; Cui, X.; Shi, J. *Chem. Commun.* **2009**, 6071.
(3) Wheeler, D. A.; Newhouse, R. J.; Wang, H.; Zou, S.; Zhang, J. Z. *J. Phys. Chem. C* **2010**, *114*, 18126.
(4) Fei, J.; Cui, Y.; Yan, X.; Qi, W.; Yang, Y.; Wang, K.; He, Q.; Li, J. *Adv. Mater.* **2008**, *20*, 452.
(5) Dai, Z.; Zhang, J.; Bao, J.; Huang, X.; Mo, X. *J. Mater. Chem.* **2007**, *17*, 1087.
(6) Xiao, L.; Zhao, Y.; Yin, J.; Zhang, L. *Chem.—Eur. J.* **2009**, *15*, 9442.
(7) Caruso, F.; Caruso, R. A.; Mohwald, H. *Science* **1998**, *282*, 1111.
(8) Cong, H.; Yu, S. *Adv. Funct. Mater.* **2007**, *17*, 1814.
(9) Yu, H.; Yu, J.; Liu, S.; Mann, S. *Chem. Mater.* **2007**, *19*, 4327.
(10) Teng, F.; Xu, T.; Liang, S.; Buergen, G.; Yao, W.; Zhu, Y. *Catal. Commun.* **2008**, *9*, 1119.
(11) Zhang, W.; Hu, J.; Guo, Y.; Zheng, S.; Zhong, L.; Song, W.; Wan, L. *Adv. Mater.* **2008**, *20*, 1160.
(12) Sberveglieri, G. *Sens. Actuators, B* **1995**, *23*, 103.
(13) Mason, T. O.; Gonzalez, G. B.; Kammler, D. R.; Mansourian-Hadavi, N.; Ingram, B. J. *Thin Solid Films* **2002**, *411*, 106.
(14) Wang, W. W.; Zhu, Y. J.; Yang, L. X. *Adv. Funct. Mater.* **2007**, *17*, 59.
(15) Brousse, T.; Retoux, R.; Herterich, U.; Schleich, D. M. *J. Electrochem. Soc.* **1998**, *145*, 1.
(16) Lou, X. W.; Wang, Y.; Yuan, C.; Lee, J. Y.; Archer, L. A. *Adv. Mater.* **2006**, *18*, 2325.
(17) Han, S.; Jang, B.; Kim, T.; Oh, S. M.; Hyeon, T. *Adv. Funct. Mater.* **2005**, *15*, 1845.
(18) Du, N.; Zhang, H.; Chen, J.; Sun, J.; Chen, B.; Yang, D. *J. Phys. Chem. B* **2008**, *112*, 14836.
(19) Chen, J. S.; Li, C. M.; Zhou, W. W.; Yan, Q. Y.; Archer, L. A.; Lou, X. W. *Nanoscale* **2009**, *1*, 280.
(20) Liu, J.; Xia, H.; Xue, D.; Lu, L. *J. Am. Chem. Soc.* **2009**, *131*, 12086.
(21) Wang, Y.; Su, F.; Lee, J. Y.; Zhao, X. S. *Chem. Mater.* **2006**, *18*, 1347.
(22) Lou, X. W.; Deng, D.; Lee, J. Y.; Archer, L. A. *Chem. Mater.* **2008**, *20*, 6562.
(23) Lou, X. W.; Li, C. M.; Archer, L. A. *Adv. Mater.* **2009**, *21*, 2536.
(24) Lin, Y.; Duh, J.; Hung, M. *J. Phys. Chem. C* **2010**, *114*, 13136.
(25) Wu, P.; Du, N.; Zhang, H.; Yu, J.; Yang, D. *J. Phys. Chem. C* **2010**, *114*, 22535.
(26) Wu, P.; Du, N.; Zhang, H.; Yu, J.; Yang, D. *J. Phys. Chem. C* **2011**, *115*, 3612.
(27) Yin, Y.; Rioux, R. M.; Erdonmez, C. K.; Hughes, S.; Somorjai, G. A.; Alivisatos, A. P. *Science* **2004**, *304*, 711.
(28) Fan, H. J.; Gosele, U.; Zacharias, M. *Small* **2007**, *3*, 1660.
(29) Wang, Y.; Cai, L.; Xia, Y. *Adv. Mater.* **2005**, *17*, 473.
(30) Du, N.; Zhang, H.; Chen, B.; Ma, X.; Yang, D. *Chem. Commun.* **2008**, 3028.
(31) Smigelskas, A. D.; Kirkendall, E. O. *Trans. AIME.* **1947**, *171*, 130.
(32) Sun, X. M.; Liu, J. F.; Li, Y. D. *Chem. Mater.* **2006**, *18*, 3486.
(33) Sun, X. M.; Li, Y. D. *Langmuir* **2005**, *21*, 6019.
(34) Lou, S.; Wang, J.; Zhong, C.; Rahman, M. M.; Liu, H.; Dou, S. *Electrochim. Acta* **2009**, *54*, 7519.
(35) Lou, X. W.; Chen, J. S.; Chen, P.; Archer, L. A. *Chem. Mater.* **2009**, *21*, 2868.
(36) Deng, D.; Lee, J. Y. *Chem. Mater.* **2008**, *20*, 1841.
(37) Zhang, W.; Hu, J.; Guo, Y.; Zheng, S.; Zhong, L.; Song, W.; Wan, L. *Adv. Mater.* **2008**, *20*, 1160.
(38) Yang, R.; Zhao, W.; Zheng, J.; Zhang, X.; Li, X. *J. Phys. Chem. C* **2010**, *114*, 20272.
(39) Deng, D.; Lee, J. Y. *Angew. Chem., Int. Ed.* **2009**, *48*, 1660.
(40) Lou, X. W.; Chen, J. S.; Chen, P.; Archer, L. A. *Chem. Mater.* **2009**, *21*, 2868.